

Large eddy simulation of turbulent flows via domain decomposition techniques. Part 2: applications

C. Benocci¹, R. Giammanco¹, Marcello Manna^{2,*},† and E. Simons¹

¹*von Kármán Institute for Fluid Dynamics, Department of Environmental and Applied Fluid Dynamics, Chaussée de Waterloo 72, B-1640 Rhode St. Genese, Belgium*

²*Università di Napoli 'Federico II', Dipartimento di Ingegneria Meccanica per l'Energetica, via Claudio 21, 80125, Naples, Italy*

SUMMARY

The present paper discusses the application of large eddy simulation to incompressible turbulent flows in complex geometries. Algorithmic developments concerning the flow solver were provided in the companion paper (*Int. J. Numer. Meth. Fluids*, 2003; submitted), which addressed the development and validation of a multi-domain kernel suitable for the integration of the elliptic partial differential equations arising from the fractional step procedure applied to the incompressible Navier–Stokes equations. Numerical results for several test problems are compared to reference experimental and numerical data to demonstrate the potential of the method. Copyright © 2005 John Wiley & Sons, Ltd.

KEY WORDS: LES; DNS; domain decomposition; boundary layer; backward-facing step; square cylinder flow

1. INTRODUCTION

Numerical simulation of turbulent flows can be achieved applying direct numerical simulation approach (DNS), where all the relevant scales are numerically resolved, or large eddy simulation approach (LES), where only the largest and anisotropic scales are resolved, while the smallest ones are modelled by an *ad hoc* model [1]. These procedures are beginning to be considered mature for application to flows more complex than simple *building block* flows, whose simulation has justified their success and diffusion as reliable turbulence research tools. In this frame, the term *complexity* covers both challenging physical problems (e.g. involving phase changes, combustion, shocks and acoustics to name a few) as well as flows in geometries

*Correspondence to: Marcello Manna, Università di Napoli 'Federico II', Dipartimento di Ingegneria Meccanica per l'Energetica, via Claudio 21, 80125, Naples, Italy.

†E-mail: manna@unina.it

of increased complexity (e.g. blunt and bluff body flows in composite configurations). These issues may, and usually do, occur simultaneously making it difficult, if not impossible, to consider them separately.

The latest achievements in the field of simulation have been made possible by the rapid advancements of the ready-to-use hardware technology and the combined progresses of the numerical algorithms and sub-grid stress closures [1,2]. In particular, LES is considered, in some parts, to be mature for industrial applications, as witnessed by the introduction of this technique in commercial software packages [3]. Nevertheless, we must reckon that, despite impressive progresses in the field of LES, their application to complex separated flows remains an extremely challenging task, as shown by results and conclusions of recent workshops [4].

While not disregarding the need for further improvements of the sub-grid models, one of the key issues, which justifies due attention, is the efficient solution of the elliptic kernel arising from the temporal discretization of the incompressible governing equations. In this frame, we consider that, in flow problems where geometry includes sharp edges of rectangular shapes, no practical alternative exists, at least in the structured grid context, to the application of the multi-domain (MD) technique.

This approach allows to decouple the original problem in a set of two sub-problems, *viz.* a sub-domain problem and an interface condition. The evident advantages of this procedure lie in the easiness of the description and discretization of complex geometries, good grid control, feasibility of parallel execution on multi-node computers, and, *fundamentally*, the possibility to work on simple sub-domains where fast elliptic solvers (FES) could be applied. Furthermore, MD approach is naturally suited for the application of zonal techniques, where optimal algorithms and models can be applied to different parts of the computational field. A partial example of this capability will be shown in Section 6.

The companion paper [5] has discussed our proposed approach for a strategy of decomposition of the elliptic kernel over non-overlapping sub-domains, which extends the use of fast direct and iterative elliptic solvers to any geometry made by an arbitrary collection of rectangular sub-domains. Present contribution concerns the application of this technique to LES of complex flows, providing the reader with a complete overview of its performance and capabilities.

The article is organized as follows: test cases chosen to validate the proposed numerical procedure [5] are first presented in Section 2. Boundary conditions for space-developing flows are then detailed in Section 3. Section 4 presents the results for the simulation of a spatially developing turbulent boundary layer, carried out with an innovative procedure for the generation of appropriate inflow data. Section 5 describes the application of the present technique to the simulation of the backward-facing step flow. Finally, Section 6 presents the simulation of flow over a cylinder with square cross-section. Conclusions and assessment of performance of the present approach are given in Section 7.

2. TEST CASES

Test cases chosen for this investigation have been selected to put in evidence different advantages of the present MD approach for LES of space-developing flows. They are listed below in order of increasing complexity.

- *Turbulent boundary layer flow.*

The turbulent boundary layer flow (TBL) over a flat plate is a highly important building block flow for fundamental research. In fact, it represents the simplest case of space-developing flow, where statistic homogeneity is only present in the spanwise direction, so that separated upstream and downstream boundary conditions must be applied in the streamwise direction. It will be shown that the present approach offers an elegant and efficient imposition of realistic conditions to the upstream boundary of the computational domain. Furthermore, TBL is a first example of a semi-confined flow, with challenging problems related to boundary condition implementation at the remaining open boundaries, *viz.* the free stream top boundary and the outflow boundary.

- *Backward-facing step flow.*

Backward-facing step (BFS) is the simplest example of flow separation over a sharp corner and has, therefore, become a widely studied benchmark case for CFD. In particular, availability of DNS data for BFS flow at moderate Reynolds number [6] represents an excellent opportunity to validate and assess the performances of LES codes [7]. In spite of apparent simplicity of this geometry, detailed simulations of this flow in separated and recovering regions still remain a challenging task for any numerical approach. Specifically, the simulation should be able to reproduce the particular effects put in evidence by DNS, such as the extremely low minimum value found for skin friction C_f within the re-circulation region and the extreme slow recovery towards equilibrium for the boundary layer downstream of reattachment point. Both observations seem to be due to low Reynolds number effects.

- *Cylinder of square cross-section.*

Flow around a cylinder of square cross-section (CSCS) is the simplest test case where the full phenomenology of bluff body aerodynamics can be encountered and simulated. In fact, this flow is one of two benchmark cases considered in the already quoted workshop [4] and has been adopted as a standard benchmark of validation of LES [7]. Flow around this body is characterized by multiple separated and re-developed regions. Incoming flow separates itself on the upstream corners, to give birth to two symmetric re-circulation regions over the two faces parallel to the main flow; these separated regions interact and merge with the separation region on the downstream face of the body. Downstream of the base separated region, the flow re-organizes itself in an unsteady wake, dominated by vortex-shedding from the two trailing edges. The complexity of the flow allows to take full advantage of MD formulation to resolve the regions close to the body and the development of the wake. Available reference experimental data [7, 8] allow in depth validation of present results.

3. BOUNDARY CONDITIONS

Numerical methods and interface treatment for both momentum equations and elliptic pressure kernel have already been extensively discussed in Reference [5], and thus will not be discussed here. On the contrary, boundary conditions, which are relevant for present test cases, will be, instead, specifically addressed.

In the following, periodic conditions will always be imposed in spanwise y direction, leaving the formulations for *inlet*, *outlet*, *free flow* and *wall* conditions to be discussed.

3.1. Upstream boundary conditions

As already stated, in case of space-developing flows, periodicity conditions cannot be applied in the direction of development, and separated upstream and downstream boundary conditions must be, therefore, considered. Focusing, for now, on upstream boundary, it must be said that the choice of satisfactory condition for TBL and, more in general, for flows around a bluff body, is not a problem of easy solution.

In case of bodies immersed in boundary layers, *natural* development of boundary layer flow would require huge resources [9]; therefore, practical simulations would require the flow at upstream boundary to be representative of developed turbulence. In case of the flow around a free body, many researchers [4] have assumed incoming flow to be laminar and allowed turbulence to develop itself from the separation points; however, there are reasons to suspect that lack of upstream turbulence could partly explain discrepancies found between experimental data and simulations [4], pointing again to the general need for upstream boundary conditions which are fully turbulent and have the correct correlations.

This requirement cannot be satisfied by the application of random perturbations superposed to a steady mean flow, simply because these fluctuations tend to die down over a short downstream length; artificially correlated fields have been proposed in the literature, but they can be considered an *ad hoc* solution unlikely to provide a general method. The most common approach lies with the application of results from a *precursor* LES calculation for a flow at equilibrium, having the same Reynolds number and characteristic lengths as the flow case to be simulated; in this precursor calculation, a cross plane (*slice*) is extracted at each time step and used as upstream condition for the space-developing flow. The two calculations must be performed with the same time step to ensure the compatibility of the two flow fields, typical examples of precursor flow being channel flow for internal flows, and boundary layer at equilibrium for external ones. An obvious drawback of the method is that the computer resources necessary to produce the slices must be added to the cost of the full calculation. However, in case of complex flows, this cost is not likely to be a very significant overhead. As title of example, Figure 1 shows the application of this technique to the simulation of TBL over a flat plate, where an equilibrium *half-channel*, with a Neumann condition (see below)

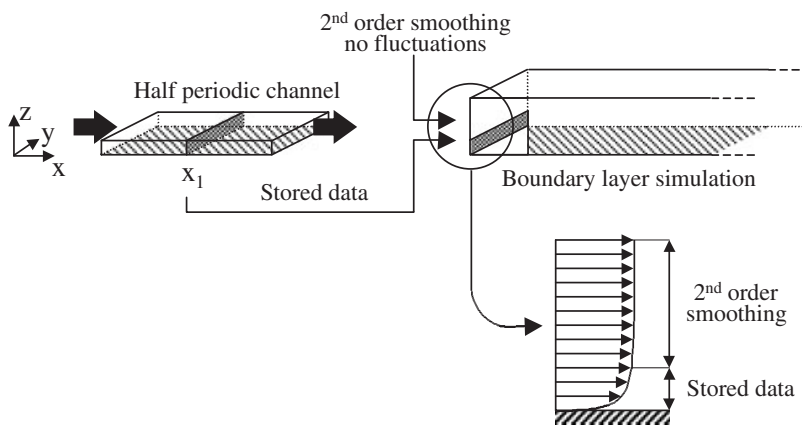


Figure 1. Inflow data generator technique.

at the top boundary, and periodic boundaries in the streamwise direction, is used as precursor. Application of the MD technique in parallel environment allows an elegant improvement to this approach: in fact, the current parallel MD solver permits to run simultaneously the pre-simulation and the post-simulation through the addition of a single dedicated boundary condition routine.

The pressure and velocity boundary conditions for the pre-simulation sub-domain remain unchanged, whereas for the main simulation the boundary conditions at the inflow boundary sub-domains are modified to receive data from the corresponding sub-domains of the pre-simulation. Practically, a dedicated sub-routine copies velocity and pressure data of an internal cross-plane (far from the region of influence of the streamwise periodic condition for the precursor) of the inflow generator simulation at the end of every time step and pass them at the inflow boundary of the post-simulation. This step removes any need for storing typically huge amounts of data on disk, since the instantaneous inflow data are produced *on the fly* as part of the complete simulation. The incorporation of a simultaneously run pre- and post-simulation is a simple matter using current MD solvers, since both the pre- and post-simulation sub-domains are designed during the domain partitioning step and internally coupled in a straightforward manner.

3.2. Free stream boundaries

In flow problems, which feature a developing boundary layer unbounded in the vertical direction, boundary condition must model the interaction of the developing boundary layer with the external asymptotic flow. In the current study, the free stream boundary condition has been adopted:

$$u = u_{\infty}, \quad \frac{\partial v}{\partial z} = 0, \quad \frac{\partial w}{\partial z} = 0 \quad (1)$$

For cases of flow around bodies in free flight, the computational field is limited by the related condition

$$\frac{\partial u_i}{\partial x} = 0 \quad (2)$$

3.3. Convective outflow boundaries

At the outflow boundary, convective boundary conditions are applied in order to cause minimal disturbance to the flow upstream of the outflow plane. A one-dimensional pure convection equation is used for each of the three velocity components:

$$\frac{\partial u_i}{\partial t} + U_c \frac{\partial u_i}{\partial x} = 0 \quad (3)$$

The streamwise bulk velocity U_{bulk} has been adopted as the choice for the convection velocity U_c .

The convective outflow boundary conditions are discretized using an implicit Euler formula in time and a 1st order upwind formula in space.

In a two-dimensional steady setting the convective boundary conditions cause the streamlines at the outflow domain to lie parallel to the x -axis. Therefore, it is advisable, whenever these boundary conditions are applied, to locate the outflow boundary sufficiently far away

from any region in the flow with an important mean streamline curvature, as, for instance, the recirculating region of a separated flow.

3.4. Mass correction

Due to the approximate nature of the present boundary treatment at open boundaries, at each time step, a small mass-flow imbalance may be introduced. Whenever using an iterative pressure-Poisson solver and failing to correct adequately for this mass flow imbalance, a significant deterioration of the convergence speed and a lack of convergence, altogether, usually occurs. This behaviour can be directly linked to the violation of the compatibility condition which no longer guarantees the existence of the Poisson solution. It has been found crucial for the long-time stability of the temporal integration, to introduce a *mass-correction* mechanism which is applied at each time step of the numerical integration to remedy for this slight violation of the mass conservation principle.

Therefore, an additive correction factor ε is subtracted from the RHS of the convective outflow boundary formula presented in Equation (3) for the streamwise velocity. The ε term is given by

$$\varepsilon = \dot{m}_{\text{outfl}} + \dot{m}_{\text{top}} - \dot{m}_{\text{infl}} \quad (4)$$

and the respective mass fluxes are defined as

$$\dot{m}_{\text{outfl}} = \iint_{A_{\text{out}}} u_{\text{outfl}}^{n+1} dy dz \quad (5)$$

$$\dot{m}_{\text{top}} = \iint_{A_{\text{top}}} w_{\text{top}}^{n+1} dx dy \quad (6)$$

$$\dot{m}_{\text{infl}} = \iint_{A_{\text{infl}}} u_{\text{infl}}^{n+1} dy dz \quad (7)$$

This formulation introduces the required net source/sink of mass into the computational domain at the new time step $n + 1$.

3.5. Wall boundary conditions

The natural boundary condition of a flow on a solid wall is the *no-slip* condition. However, its application to turbulent flows presents strong practical difficulties related to the physical nature of turbulence close to a wall. For flows at, or close to equilibrium, the near wall flow can be thought divided [10, 11] in two regions, *viz.* a viscous sub-layer, where viscous transport is bigger than turbulent effects and a region of developed turbulence, where laminar viscosity and diffusivity play a small role with respect to the turbulent transport of momentum and energy. Between the two, a buffer zone lies, where continuous transition from the former to the latter behaviour takes place. Low-order finite difference discretization can represent no-slip condition only where the velocity profile is linear, or, in other terms, within the viscous layer ($z^+ \leq 5$). Therefore, direct imposition of this condition would require a grid refined enough to resolve viscous and buffer layers. A minimal resolution requirement for the direction normal to the wall is that three grid points are located within the first 10 wall units [12]. The requirements in the two directions parallel to the wall are less strict, but

still significant, due to the need to resolve the longitudinal streaks, which are responsible for turbulence production [13]. Literatures [12, 14] suggest that maximal acceptable grid size is in order of 80 wall units for the streamwise direction and 30 for the spanwise one. Direct experience of present authors is that, in case of 2nd order finite difference discretization, grid spacings of half these sizes are a minimum to reproduce the dynamics of the inner layer [15].

It is clear that, with increasing Reynolds number, this requirement becomes impossible to satisfy. Matter of fact, the number of grid points necessary for resolved LES increases with $Re^{1.8}$ for viscous and buffer layer and $Re^{0.4}$ for the part of the flow outside them [16]. Considering complex three-dimensional flows at $Re = 10^6 - 10^8$, this condition clearly exceeds the capabilities of present or expected computers. Therefore, application of LES to high Re flows requires to renounce to resolve the layer close to the wall and model it by simpler (and hence less accurate) approaches [17], while full LES must be confined to regions of developed turbulence.

However, the purpose of the present study being to assess and demonstrate the capability of the MD approach over well documented test cases, the investigation is confined to Re number flows such that no-slip conditions can be directly applied.

4. SPACE-DEVELOPING TURBULENT BOUNDARY LAYER

As stated in Section 2 the TBL developing over a flat plate is a building block flow of major fundamental importance in the understanding and modelling of turbulence. Availability of reliable DNS data [18] makes this case ideally suitable to validate the approaches introduced in Reference [5] and in Section 3. A schematic view of the flow is presented in Figure 2. Classical definitions are introduced for the local boundary layer thickness $\delta(x)$, defined as the z location where the local velocity u takes the value $u = 0.99u_\infty$, for the local displacement thickness, $\delta_1(x) = 1/u_\infty \int_0^\infty (u_\infty - u) dz$, and for the local momentum thickness, $\delta_2(x) = \int_0^\infty u/u_\infty (1 - u/u_\infty) dz$. The corresponding Reynolds numbers:

$$Re(x) = \frac{\delta(x)u_\infty}{\nu}, \quad Re_1(x) = \frac{\delta_1(x)u_\infty}{\nu}, \quad Re_2(x) = \frac{\delta_2(x)u_\infty}{\nu}$$

will be applied for the analysis of present simulation.

The test case is the zero pressure gradient TBL developing over a flat plate. The simulation is designed to match available DNS data by Spalart [18] at $Re_1 = 2000$ ($Re_2 = 1410$) and experimental data by Antonia [19] at $Re_1 = 2200$ for this flow.

The computational field, shown in Figure 3, is chosen to simulate boundary layer at $Re_1 = 2000$, which leads to sizes of streamwise, spanwise and wall-normal lengths of $24\delta_{\text{inlet}}$, $\pi/2\delta_{\text{inlet}}$ and $3\delta_{\text{inlet}}$, respectively. Values of spanwise and wall-normal sizes of the domain are largely guided by the previous LES study performed by Lund *et al.* [20]. The streamwise length was chosen to allow the flow to recover from any mismatching due to approximate inflow data and, at the same time, to maintain a sufficient separation between the streamwise location where data will be extracted and the one where outflow boundary conditions will be imposed, to prevent the contamination of the solution.

As stated, the aim of the simulation is to attain the Reynolds number regime $Re_1 = 2000$, preferably somewhere close to the middle of the computational domain ($x \approx 12\delta_{\text{inlet}}$). Therefore, the Reynolds number of the pre-simulation has to be guessed on the basis of the

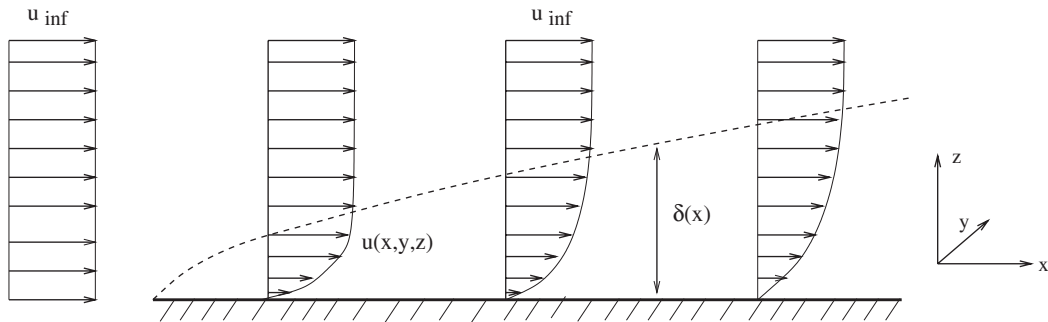


Figure 2. Sketch of a boundary layer developing over a flat plate, including the visualization of the boundary layer thickness δ .

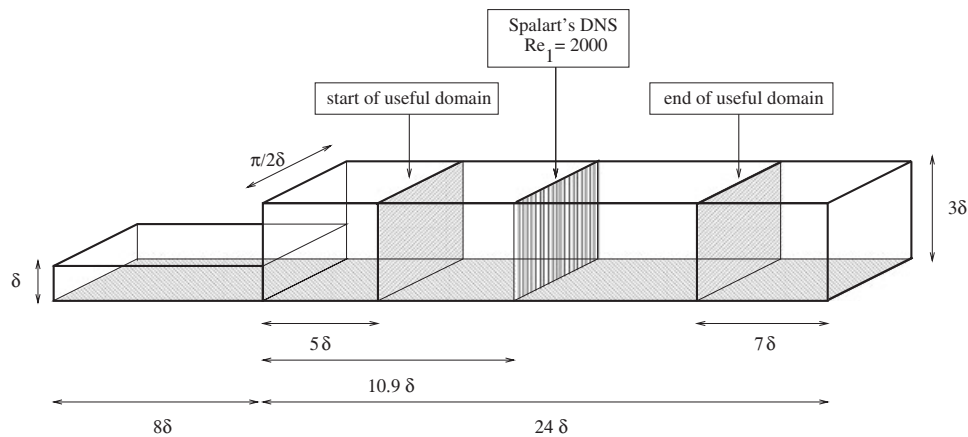


Figure 3. Computational domain for the turbulent boundary layer and for the half channel pre-simulation. Locations of the points of comparison with the reference data and of the delimiters of useful region.

standard theoretical/empirical laws for the streamwise boundary layer thickness development, such as those given in Equations (8) and (9). On this basis, the Reynolds number of the half-channel pre-simulation was then chosen to be $Re = u_{\text{bulk}} L_z^{\text{prech}} / \nu = 9650$, which corresponds with $Re = u_{\infty} \delta_{\text{inlet}} / \nu = 11238$ using the identities $L_z^{\text{prech}} = \delta_{\text{inlet}}$ and $u_{\infty} / u_{\text{bulk}}^{\text{prech}} = 1.16$. In Figure 3, the streamwise location $x = 10.9 \delta_{\text{inlet}}$ where LES results are compared with the DNS data set [18] at $Re_1 = 2000$ is marked. The computational domain is discretized with a uniform grid spacing in the streamwise and spanwise directions, whereas a hyperbolic tangent stretching function was applied in the wall-normal direction to resolve the turbulent structures close to the wall. Information concerning grid size and resulting resolution in wall units are resumed in Table I. Again the chosen resolution was guided by the LES study of Lund *et al.* [20] and by the need to ensure a wall resolved simulation. As discussed in Reference [5], Smagorinsky's closure for the sub-grid-scale stresses with $C_s = 0.1$, is applied for the entire computational field, while Van Driest damping is applied close to the solid wall, to account for the cor-

Table I. Turbulent boundary layer simulation parameters summary.

	TBL
$Re_{\text{bulk}}^{\text{prech}}$	9650
Re	11238 \rightarrow 16027
Re_1	1665 \rightarrow 2412
Re_2	1227 \rightarrow 1749
(L_x, L_y, L_z)	$24\delta_{\text{inlet}} \times \frac{\pi}{2}\delta_{\text{inlet}} \times 3\delta_{\text{inlet}}$
Grid	$240 \times 64 \times 45$
Tot. Cells	691200
z stretching	hyperbolic tangent
$\Delta x_i/\delta_{\text{inlet}}$	$0.1 \times 0.0245 \times (0.00374: 0.178)$
$\Delta x_{i,\text{meas.loc.}}^+$	$52.8 \times 12.9 \times (1.975: 94)$

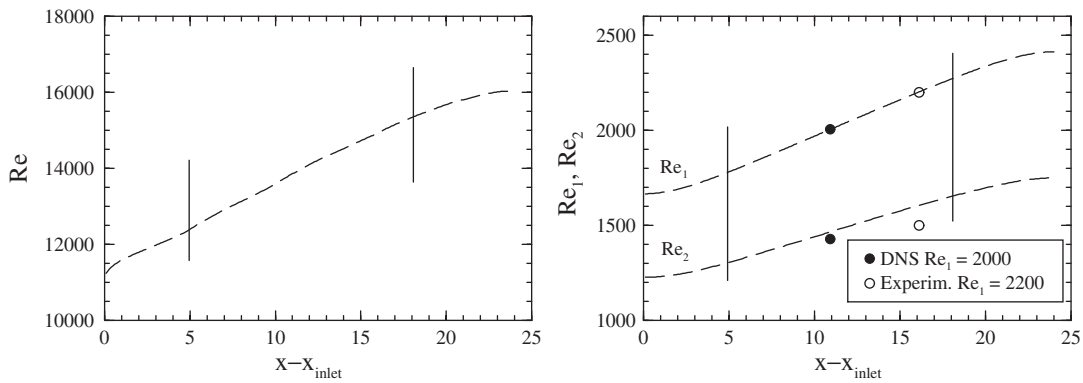


Figure 4. Spatial evolution of the boundary layer in terms of Re , Re_1 , Re_2 ; comparison of LES results with Spalart’s DNS data (1988) and with Antonia’s experimental data (1981) at the chosen locations.

rect decrease in turbulence length scales [21]. In Figures 4–6 we compare current LES results for the streamwise development of δ , δ_1 , δ_2 and τ_{wall} with aforementioned DNS data [18], experimental data [19] and classical semi-empirical correlations [22] resumed in Equations (8)–(11).

$$\delta(x) = 0.37x \left(\frac{u_\infty x}{\nu} \right)^{-1/5} = 0.37x^{1/5} \left(\frac{Re_{\text{inlet}}}{\delta_{\text{inlet}}} \right)^{-1/5} \tag{8}$$

$$\delta_1(x) = \frac{1}{8} \delta(x) \tag{9}$$

$$\delta_2(x) = \frac{7}{72} \delta(x) \tag{10}$$

$$\frac{\tau_w(x)}{\rho u_\infty^2} = \frac{1}{2} C_f(x) = 0.0128 \left(\frac{u_\infty \delta_2(x)}{\nu} \right)^{-1/4} = 0.02292 \delta(x)^{-1/4} \left(\frac{Re_{\text{inlet}}}{\delta_{\text{inlet}}} \right)^{-1/4} \tag{11}$$

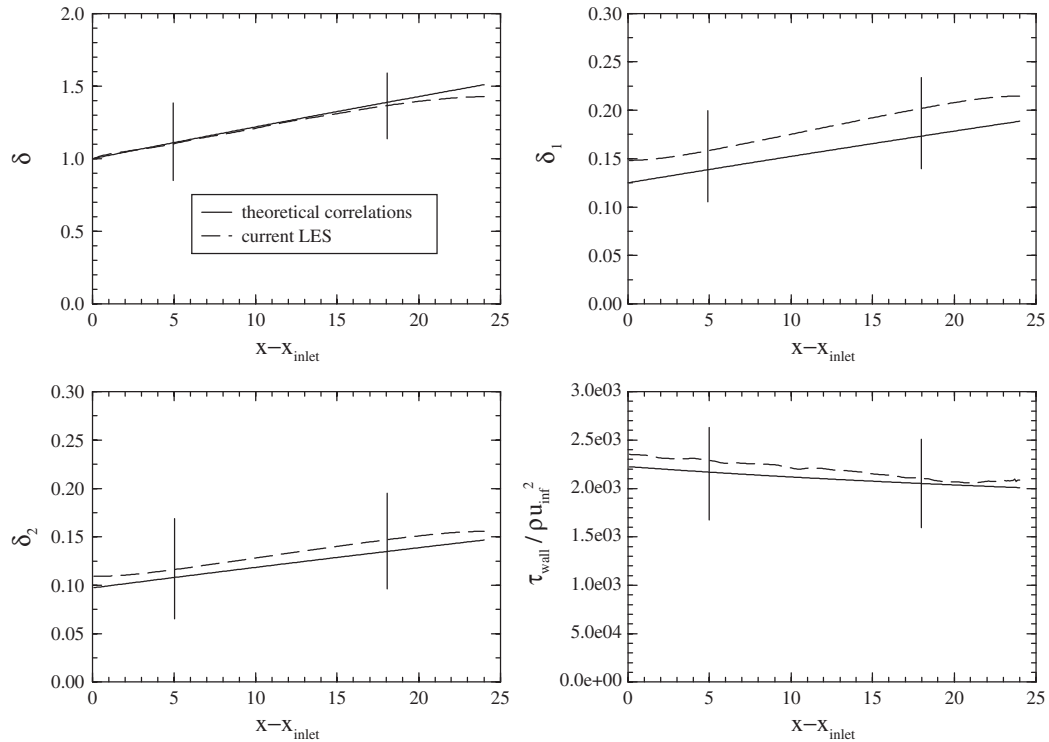


Figure 5. Spatial evolution of the boundary layer thickness (δ), displacement thickness (δ_1), momentum thickness (δ_2) and wall shear stress (τ_{wall}); comparison with semi-empirical correlations (Schlichting).

From Figure 4 we observe that in the present simulation the Reynolds numbers based on displacement thickness Re_1 will match both the DNS and experimental data, while, the result for the Re_2 case lies above the reference values, with a larger disagreement concerning the experimental data. As a consequence, the shape factor of the boundary will be slightly different from the target one.

The prediction of the boundary layer growth rate compares very well with the one pertaining to the semi-empirical correlation, as it can be appreciated from Figure 4, whereas the slope of the evolution of wall shear stress is slightly steeper than the one predicted by the theoretical correlation. Perhaps, the most important information to be gathered from Figure 4 concerns the estimation of the useful region of the current calculation. Deviation from the uniform slope of the respective graphs at the beginning and end of the domain allows to delimit the streamwise length which is necessary for the simulated flow to recover from the approximate inflow data and the upstream length over which it is influenced by the effects of convective outflow boundary condition. We could estimate the inflow recovery length to be less than $5\delta_{\text{inlet}}$, whereas the influence of the outflow boundary conditions seems to extend up to $7\delta_{\text{inlet}}$ upstream of the outflow boundary. In both figures the corresponding positions are indicated by a vertical bar. These results lead to the conclusion that the current inflow boundary technique needs a relatively short recovery length, compared to other possible

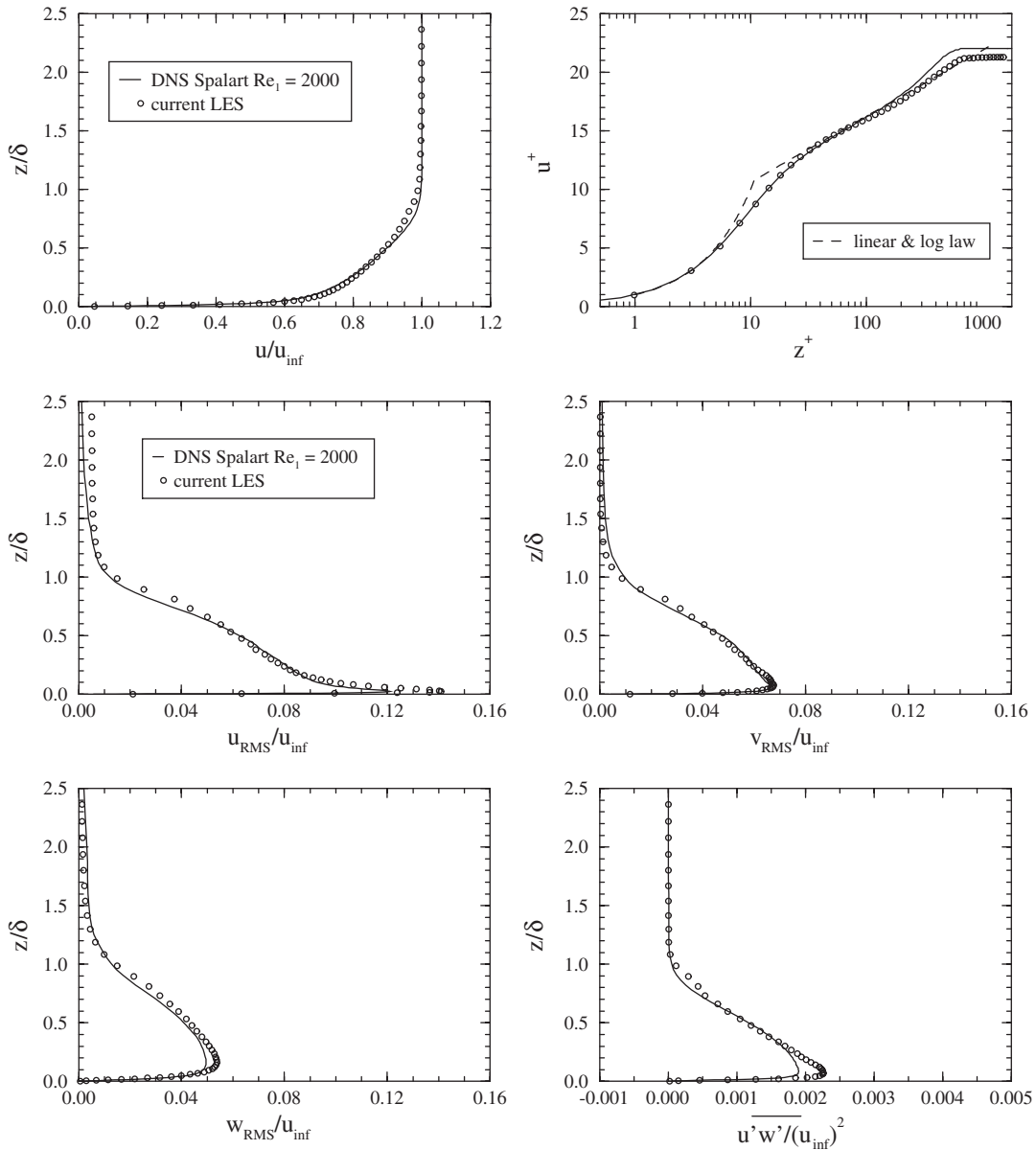


Figure 6. Comparison between Spalart's DNS data at $Re_1 = 2000$ (1988) and LES results at fixed Re_1 . Mean velocity (in bulk and wall units) and rms of resolved fluctuations.

techniques [20], making it a very efficient approach to the simulation of boundary layer-type flows. In Figure 6 we compare profiles at the location ($x = 10.9\delta_{inlet}$) where $Re_1 = 2000$, with DNS data at the same Reynolds number. The mean streamwise velocity profile, set in outer units, is fairly well reproduced, even though the data seem to suggest a slight difference in

the estimation of the boundary layer thickness δ . The streamwise velocity profile set in inner coordinates compares very well with DNS close to the wall, whereas above $z^+ = 200$ current results deviate from the DNS results and follow closely the *linear-log* law [22], which can be considered encouraging. The maximum value of the streamwise turbulence intensity close to the wall is over-predicted by $\approx 16\%$ with respect to the DNS, whereas the values of the rms for spanwise and wall-normal components reproduce more closely the DNS data. The total shear stress maximum is also over-predicted by $\approx 14\%$. In view of the grid resolution at the measurement location (Table I) it is estimated that this over-prediction can most likely be attributed to insufficient grid resolution in conjunction with the numerical errors associated with 2nd order finite difference scheme. However, the quality of results is comparable to those for corresponding simulations and is sufficiently accurate to demonstrate the efficiency of the present approach with semi-confined flows.

5. FLOW OVER A BACKWARD-FACING STEP

The configuration chosen for the simulation of the backward-facing step is made of a single-sided expansion duct, with expansion ratio of $H/(H - h) = 1.2$, where H is the total height of the domain behind the step expansion and h is the step height (Figure 7). The Reynolds number, based on the free stream velocity U_0 of incoming developing turbulent boundary layer and h , is 5100. The incoming flow is a boundary layer, whose thickness δ was found, by DNS [6], to be in the order of $1.2h$, at location $x = -0.3h$ upstream the corner. In the present simulation the computational field is divided into three logical parts, made of five sub-domains, which are shown in Figure 8. The technique of concurrent pre-simulation is applied to create the upstream boundary condition. In the present set-up, the first sub-domain corresponds to an equilibrium *half-channel* with no-slip wall at the bottom boundary, a slip wall at the top boundary, and periodic boundaries in streamwise direction. This sub-domain, Ω_1 , of length $L_{\text{prech}} = 9h$, acts as pre-solution to generate, in a concurrent way, inflow conditions for the actual BFS simulation. This first sub-domain is followed by a *true* inlet section, which extends itself down to the corner. This region is sub-divided into two consecutive sub-domains Ω_2 and Ω_3 of total length $L_{\text{tbl}} = 9h + 2h = 11h$. In this region, flow evolves from inflow condition to developed boundary layer. Expansion downstream of the corner covers a length $L_{\text{bfs}} = 20h$, sub-divided in two sub-domains Ω_4 and Ω_5 . In this region flow separates at the corner, re-attaches downstream on the bottom wall and evolves, again, towards a boundary layer at equilibrium. Outflow boundary is located at 20 step heights downstream of the expansion, as it is the case for DNS [6]. Free stream condition is applied to the top boundary and no-slip condition is imposed on the wall. Periodic boundary conditions are applied in the spanwise direction and the span of the computational domain $L_y = 4h$ also matches the one of the reference DNS. The total height of the post-expansion domains is $L_z = 6h$.

As mentioned in Section 3.5, the grid must be refined enough to resolve the wall layer regions, upstream and downstream of the corner, and it is, therefore, necessarily, highly stretched in both streamwise and wall-normal directions. Cell sizes for the grid adopted are resumed in Table II, expressed in terms of wall co-ordinates (on the basis of computed friction velocity at the exit of the computational domain $u_r/u_o = 3.752 \times 10^{-2}$). Resolution of the present grid is comparable to the one applied in a similar LES of this case [23]. It was found that small grid sizes and existence of high wall-normal velocity in the corner region introduce a severe time

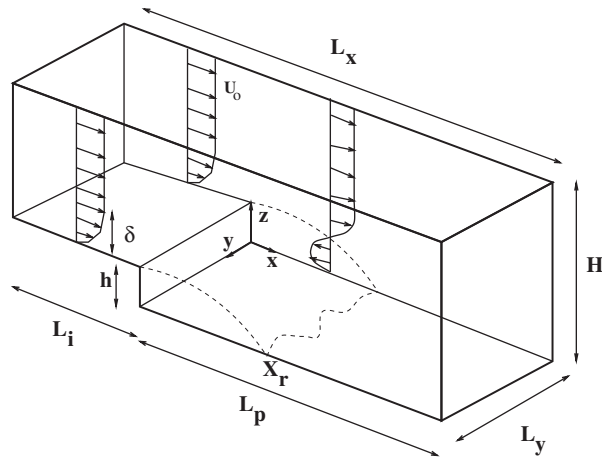


Figure 7. Schematic view of the flow over a backward-facing step, including re-circulation bubble concept. Flow from left to right.

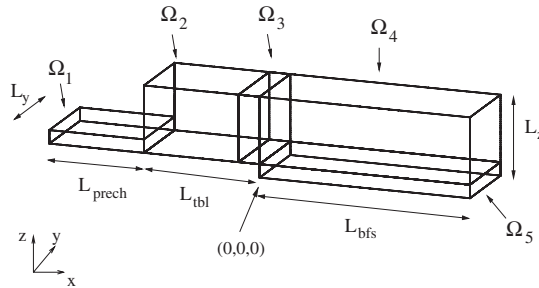


Figure 8. Multi-domain computational box for the BFS; axis not to scale.

Table II. BFS grid resolution in wall units.

	Δx_{\min}^+	Δx_{\max}^+	Δy^+	Δz_{\min}^+	Δz_{\max}^+
LES	8.61	53.7	36.1	1.1	89.0
DNS	10.4	10.4	16.7	0.3	33.2

step limitation: matter of fact, convective limit becomes stricter than the diffusive one. For current grid, the convective and viscous time step limits, in present non-dimensionalization, have been found to be:

$$(\Delta t)_{\text{conv}} = 0.004848 \quad \text{and} \quad (\Delta t)_{\text{visc}} = 0.0109$$

justifying the choice of a full explicit solver [5].

The number of grid point per sub-domain is summarized in Table III. The total amount of grid points, including half pre-channel sub-domain, is about 400 000 points. This value

Table III. Computational domain sizes and grid definition of 5 sub-domain BFS geometry.

Sub-domain	L_x	L_y	L_z	N_x	N_y	N_z
Ω_1	9	4	1.13	90	32	21
Ω_2	9	4	5	90	32	32
Ω_3	2	4	5	26	32	32
Ω_4	20	4	5	122	32	32
Ω_5	20	4	1	122	32	26

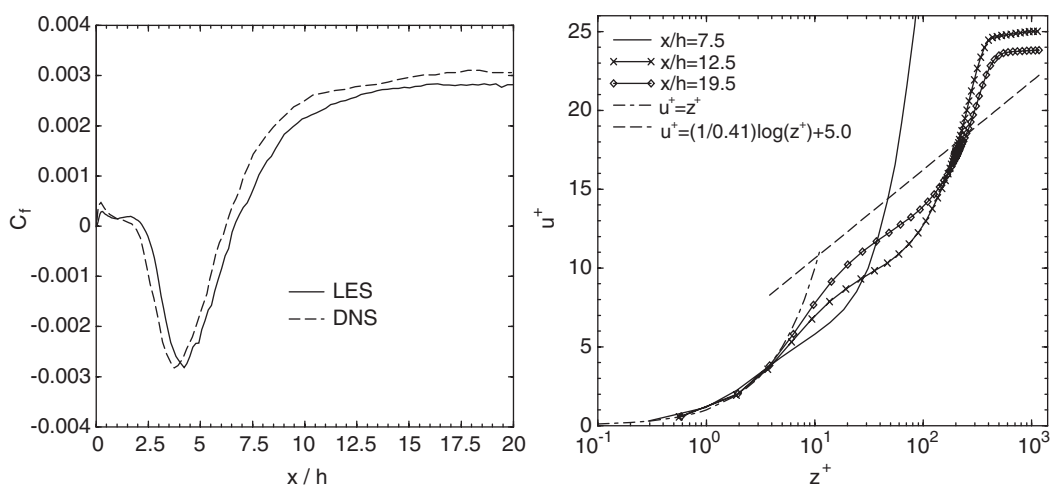


Figure 9. Skin friction coefficient downstream of the step expansion (left); evolution of the mean streamwise velocity profile in wall coordinates (right).

corresponds to less than 5% of grid-points (8 290 304) employed in DNS. The sub-grid scales are parametrized applying Smagorinsky model, with C_s coefficient set to $C_s = 0.075$, and the Van Driest damping applied on the wall regions [21].

Present simulation shows that flow upstream the corner was successfully reproduced: on the corner wall, height of boundary layer and turbulent profiles at $x = -0.3$ were found close to the corresponding values of DNS, ensuring realistic comparison for two cases. At separation, a shear layer is formed. It is bent down by the low pressure region created by the expansion and re-attaches itself on the lower wall approximately 6 step-heights downstream the corner, to give birth to a new attached wall-layer, which, slowly, re-develops towards equilibrium boundary layer flow, as shown by the evolution of the mean wall friction coefficient C_f on the bottom wall (Figure 9); existence of a counter-rotating secondary region at the bottom corner is well evident.

The comparison with DNS data shows that the length of the secondary re-circulation bubble is slightly over-predicted, which is evident in the delayed first crossing of the zero line (Figure 9). The second crossing of the zero line, corresponding to the closing of the main re-circulation region, also shows a comparable over-prediction. The predicted length of the separation region is found to be $x_R/h \approx 6.6$ against the value of $x_R/h = 6.28$ for DNS.

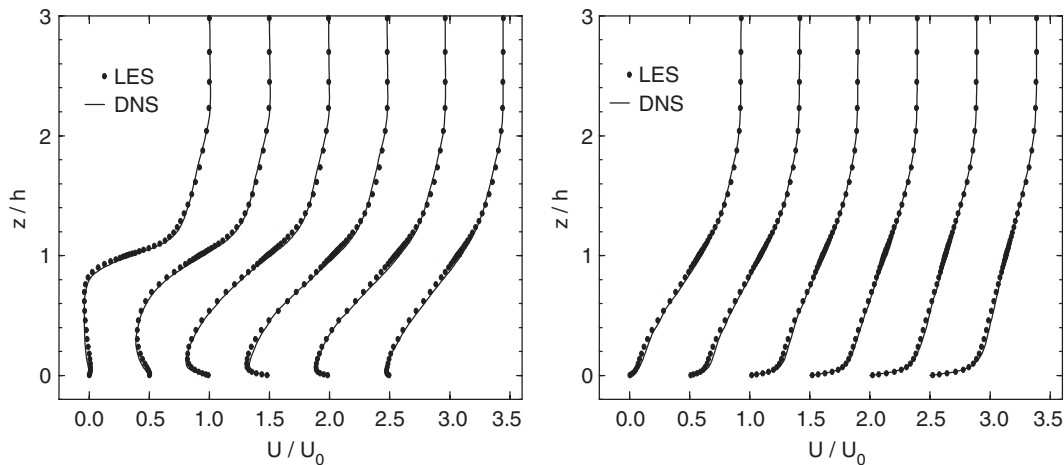


Figure 10. Mean streamwise velocity profile at $x/h = 1, 2, 3, 4, 5, 6$ (left), and $x/h = 7, 8, 10, 12, 14, 16$ (right); solid line denote DNS data from Reference [6].

The minimum value found for the friction coefficient, $C_f = -0.0028$, is identical for both calculations. This is an extremely low value, which was never observed before the DNS [6] and the accompanying experimental study [24] and, it is now, further validated by the present result.

At the outflow boundary, the wall friction is about 8% lower than the DNS value. The slowness of the recovery towards the state of equilibrium boundary layer can be observed in Figure 9 and it is remarkable that, even 20 step heights downstream the corner, profiles of mean velocity still fall well below the theoretical log-law correlation. Again, these findings are in agreement with corresponding studies [6] and [24].

Mean, rms velocity and shear stress profiles are presented in Figures 10–14 for the separation region (locations $x/h = 1, 2, 3, 4, 5$ and 6) and the re-developing boundary layer flow downstream of it (locations $x/h = 7, 8, 10, 12, 14$ and 16).

Mean streamwise velocity profiles in Figure 10, overall show a very good agreement with the DNS data, despite the small delay in the re-attachment and an over-prediction of the re-circulation length, already remarked in Figure 9. A comparable agreement is found for the mean of wall-normal velocity components (Figure 13), confirming that the mean field is well represented.

Streamwise turbulence intensity profiles, given in Figure 12, show that a maximum peak value downstream of the corner, $x/h = 1$, is well represented. This feature corresponds to the initial development of the inner shear layer emanating from the step. Further downstream, the size of this maximum is slightly over-predicted, but still close to the DNS value. Downstream of the re-attachment point, the presence of a local maximum very close to the wall puts in evidence the mechanism of a re-developing boundary layer.

The comparison of the wall-normal turbulence intensities (Figure 13) shows a similar trend. The maximum value at the first downstream position is well reproduced, but a slight over-prediction of the maximum is found for most positions further downstream. Nevertheless, overall, the agreement between two simulations is quite acceptable.

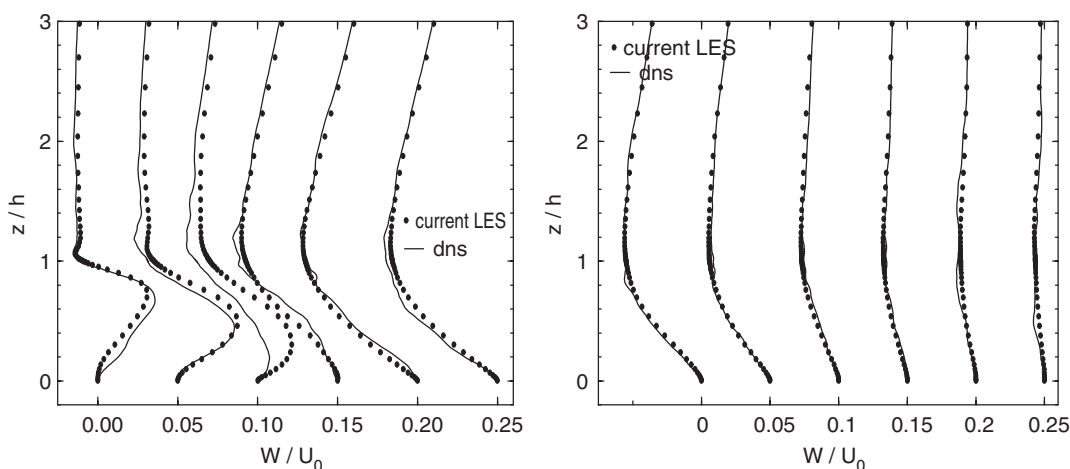


Figure 11. Mean velocity in the wall-normal direction at locations $x/h = 1, 2, 3, 4, 5, 6$ (left), and $x/h = 7, 8, 10, 12, 14, 16$ (right); solid lines denote DNS data from Reference [6].

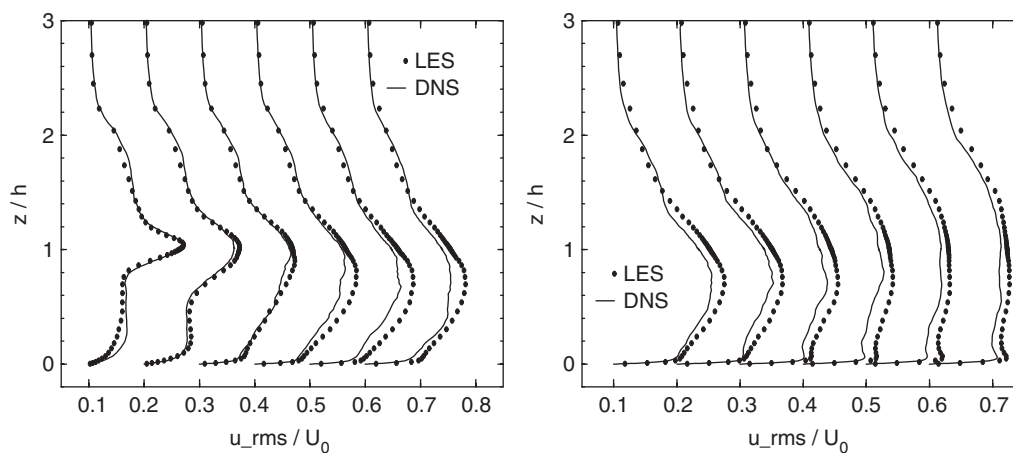


Figure 12. Streamwise turbulence intensities in the wall-normal direction at locations $x/h = 1, 2, 3, 4, 5, 6$ (left), and $x/h = 7, 8, 10, 12, 14, 16$ (right); solid lines denote DNS data from Reference [6].

Finally, the shear stress profiles are compared in Figure 14. It must be kept in mind that the shear stress here presented corresponds to the total shear stress, including the sub-grid contribution. Results match well the DNS data both upstream and downstream of re-attachment. Concerning the quality of the results, the present simulation well shows the capability of a resolved LES to yield results comparable to the DNS, with a cost 20 times smaller. The efficiency and the flexibility of the present MD solver is demonstrated by its ability to support refined, optimal grids and resolve the entire flow (precursor + *true* flow) in *one single* simulation.

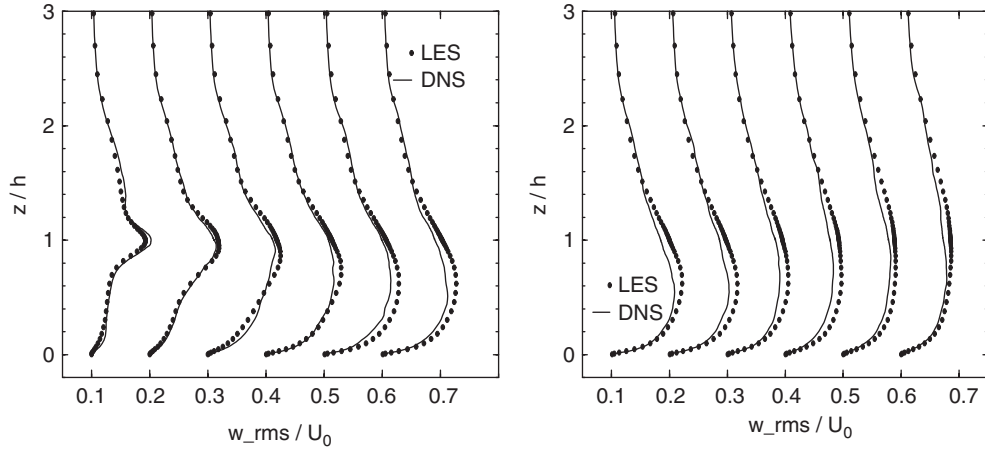


Figure 13. Normal to the wall turbulence intensities in the wall-normal direction at locations $x/h=1, 2, 3, 4, 5, 6$ (left), and $x/h=7, 8, 10, 12, 14, 16$ (right); solid lines denote DNS data from Reference [6].

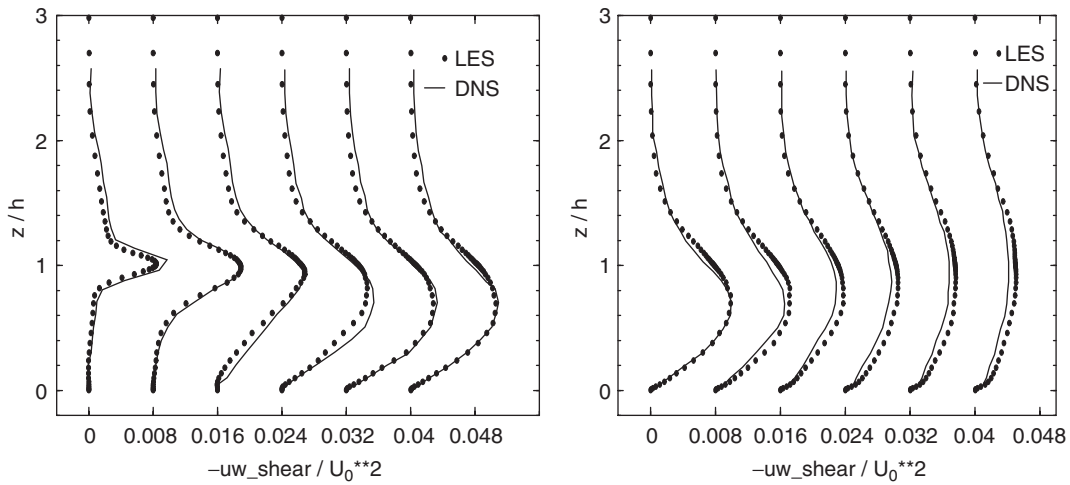


Figure 14. Shear stress profiles at $x/h=1, 2, 3, 4, 5, 6$ (left), and $x/h=7, 8, 10, 12, 14, 16$ (right); solid lines denote DNS data from Reference [6].

6. FLOW OVER A CYLINDER OF SQUARE CROSS-SECTION

As discussed in Section 2, the flow around a cylinder of square cross-section is the simplest test case where the full phenomenology of bluff body aerodynamics can be encountered and simulated. It allows to fully demonstrate the flexibility and efficiency of the MD technique. The simulation is performed at a Reynolds number $Re_H = HU_0/\nu = 22\,000$ based on the bulk velocity U_0 and the cylinder height H matching the test conditions of the experiments

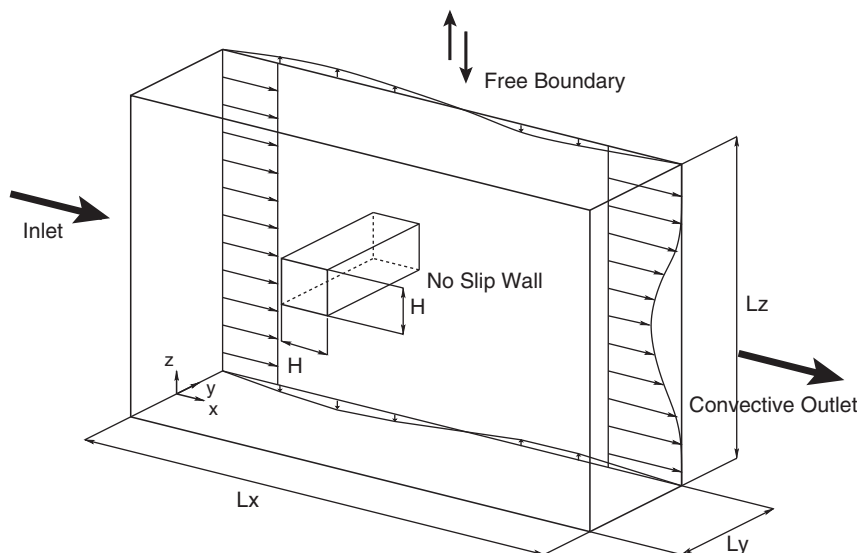


Figure 15. Flow geometry and boundary conditions for cylinder flow.

by Lyn [8]. A sketch of the computational domain for the simulation of the flow around the cylinder is presented in Figure 15 together with the corresponding boundary conditions. The computational domain matches the specifications of the aforementioned workshop [4]. Its dimensions are $22.5L_x/H$, $6L_y/H$ and $14L_z/H$, discretized over 24 sub-domains for a total $250 \times 32 \times 184 \cong 1.4 \times 10^6$ points in streamwise, spanwise and vertical direction, respectively. The spanwise resolution is possibly too coarse to fully resolve the longitudinal structures, since literature suggests 32 nodes in spanwise for $L_y/H = 4$; however, the value 6 has been chosen to ensure that the domain would be wide enough to avoid auto-excitation of the flow. A non-uniform grid in streamwise and vertical direction is obtained applying a power stretching, whose coefficients depend on the sub-domain considered. Each face of the cylinder is discretized over 60 nodes and a symmetric stretching ensures that the same gridding is applied at all the corners. The distance of the closest pressure node to the surface of the obstacle is $\cong 0.001H$ corresponding to 3.5–7.5 wall units. The stretching ratios used are rather high (up to 1.18); this choice is made necessary by the conformity of the grid across the domains. It is easy to understand how the necessity to fully resolve the wall region leads to a large amount of nodes not used thoroughly. The MD sub-division of the computational field is presented in Figure 16, where the *sophisticated* sub-division of the flow-field, made possible by the MD approach, can be appreciated; all the geometric quantities are non-dimensionalized in terms of the square cylinder side (or diameter) H .

The choice of the boundary conditions (Section 3) is driven by the need to simulate the condition of body in free flight and reproduce the experimental set-up of Reference [8]. Concerning the inlet condition, it was found necessary to apply an uniform, laminar inlet. In fact, in the experimental set-up [8], incoming flow consists of a mean uniform flow with superposed free stream turbulence; in numerical simulation of free flow, however, it is not easy to produce an inlet turbulence which is realistic in terms of spectral behaviour, energy contents,

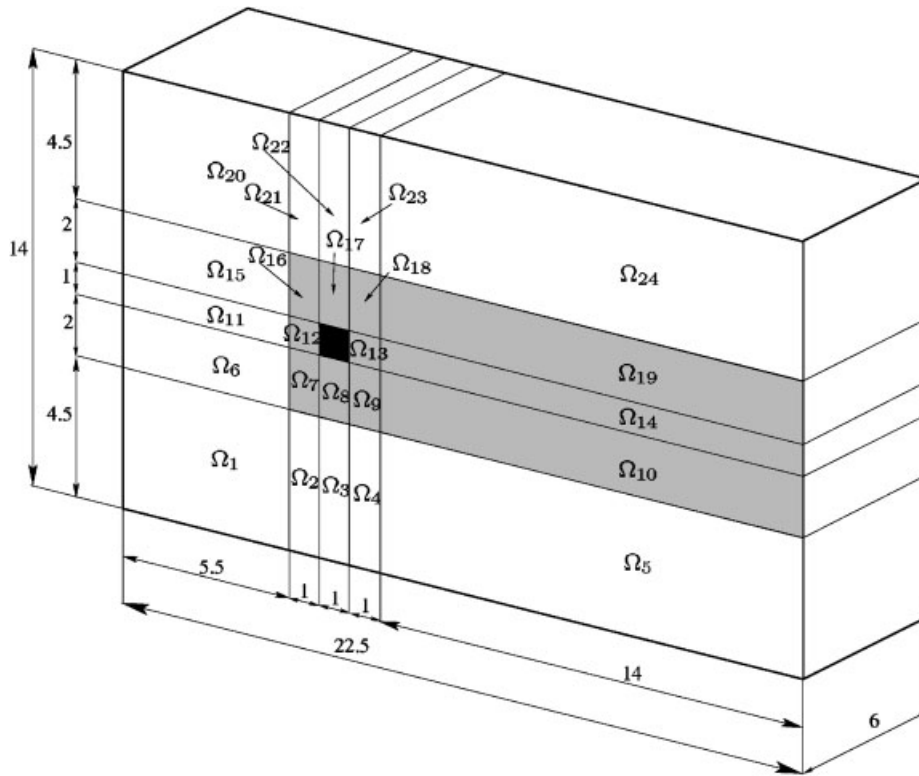


Figure 16. Multi-domain set-up for the computational field of the cylinder flow. Unshaded: 3rd order upwind treatment of convective terms without SGS modelling; shaded: 4th order central treatment of convective terms.

even applying the precursor technique, as discussed in Section 3. The simplest approach to the problem is to neglect the incoming turbulence and impose a laminar inlet. For this reason, this approach has been adopted by different groups participating to the above-mentioned workshop [4], and can be supported by the consideration that the key feature of flow development is the formation of a shear layer which detaches itself at the obstacle leading edges and downstream generates vortices shed from the trailing edges. The influence of a low level inlet turbulence can be assumed to be of small consequence on this process and, therefore, on the overall outcome of the simulation [4]. The uniform velocity U_0 , imposed at the inlet, is used to define the Reynolds number of the flow.

The top and bottom boundary locations are chosen taking into account that the reference experiments were performed in a water tunnel of blockage ratio $\frac{1}{14}$, between the tunnel and the cylinder cross-section; this ratio is reproduced in the present computational field, as shown in Figure 16. Considering the low blockage, it was considered reasonable to disregard the boundary layers developing on top and bottom walls of the test section and to apply a Neumann boundary condition for the velocity (see Section 3.2), with proper mass conservation treatment, which is obtained generalizing the procedure introduced in Section 3.4; therefore, the flow is allowed to naturally leave and re-enter the computational domain.

As already stated in Section 3, periodic conditions are applied in the transversal direction; the spanwise size of the computational field (9.8 times the size of the cross-section,) allows to consider it representative of a cylinder of infinite length. No-slip conditions are kept over the surface of the cylinder, in spite of the relative high Reynolds number. This choice is made necessary by the nature of the flow, namely by the need to well capture the detachment and re-attachment points. Even if the size of the wall cells is marginal for the application of a linear law for velocity, it is considered that the imprecision would be smaller than that pertaining to a fully approximate wall model.

In other simulations discussed in the present text (see Sections 4 and 5), all the spatial partial derivatives were discretized with 2nd order accurate centred formula. In the case of the cylinder, however, the higher Reynolds number has made necessary to introduce a 3rd order, upwind-biased discretization [25] to control aliasing errors due to insufficient dissipation. This scheme is made of the sum of a 4th order central discretization and a 4th order dissipation:

$$\frac{df}{dx} = D_{\text{central}}(f_{i\pm 2}) + \alpha D_{\text{diss}}(f_{i\pm 2}) \quad (12)$$

where $0 \leq \alpha < 1$; $\alpha = 0$ corresponds to a central 4th order scheme and $\alpha = 1$ is the full 3rd order upwind scheme. Different coefficients can be associated to the three Cartesian directions; for the spanwise direction, the value 0 is, usually, taken for the corresponding $\alpha = \alpha_y$, since the flow is periodic in that direction.

Application of an upwind-biased discretization to the convective terms adds a numerical dissipation to the viscous one and to the one generated by the SGS model, whether it is present; while this additional numerical dissipation is sometimes used to substitute the one produced by the SGS model [26], in the present instance it is introduced only because it was found to be the single way to avoid the numerical instabilities leading to the appearance of wiggles in the flow field. The problem of discretization errors is particularly strong for external flows such as the present one, where some regions of the flow can be considered to be in laminar regime, which is the case upstream the cylinder and far off the body itself and its wake; in these zones the SGS model should be disabled, either switching it off explicitly or implicitly. This is necessary for the case of Smagorinsky model, which produces a dissipation effect as soon as the resolved rate of strain is different from zero, i.e. whenever velocity gradients are present it would lead to an excessive dissipation. Therefore, the SGS terms are not computed in the sub-domains shown in Figure 16; however, the single viscous dissipation there is not able to damp out (due to high Re) the aliasing effects which would be produced by the use of a centred scheme for the convective term. Therefore, the implementation of the upwind scheme becomes indispensable. In our implementation, the coefficients α are chosen *a priori*, but the MD approach allows different values of α for different sub-domains, that can be used at the users discretion. Therefore, in these domains upwinding is applied, with the corresponding coefficients α_x and α_z (for streamwise and vertical direction) set to 0.5.

On the other hand, the SGS model is active on the central row of sub-domains downstream of the cylinder, (Figure 16) and the upwinding coefficient α is set to 0 for all the directions, so that no extra numerical dissipation is added. The vertical size of these sub-domains has been chosen to cover most of the wake development and to keep this process free of numerical effects. For the domains where the Smagorinsky model is active, the coefficient C_s is set to the constant value 0.2 on the basis of extensive testing.

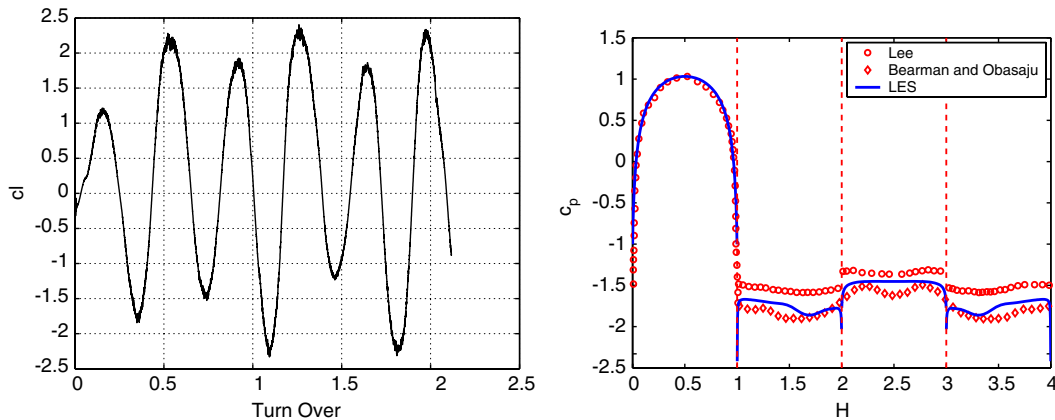


Figure 17. Pressure lift coefficient (left) and distribution of the pressure coefficient around the obstacle (right).

The analysis of the results of the simulation must consider that the flow is characterized by the shedding of spanwise vortices in an alternate fashion from the flapping shear layers generated by the upper and lower leading corners of the square cylinder. The vortices arrange themselves in a von Kármán street configuration, leading to the existence of a dominant frequency in the flow that it is usually linked to the dominant frequency of the lift coefficient. The fluid-dynamic forces acting on the obstacle are due to pressure and viscous effects; from the pressure coefficient ($c_p = 2(p - p_{\text{ref}})/0.5\rho V^2$) it is possible to extract, using a surface integral, the lift (c_l^p) and drag (c_d^p) coefficients. Since the viscous contribution to the lift and drag has not been considered in the current analysis (assuming it negligible due to high Re) the simpler c_l and c_d notations will be used.

The c_l coefficient is not influenced from the base region (the downstream face of the obstacle), and its behaviour is directly related to the shedding of the spanwise vortices. The time evolution of c_l , if the Re was sufficiently low, would be with zero mean and periodic in time; however, in the present case, Re is sufficiently high to produce turbulent motions in the wake which modify the vortex shedding behaviour by a significant amount. This could be easily observed from Figure 17; not only the shedding cycles are sufficiently different one from the other, but, moreover, low frequency phenomena seem to be present. In Figure 17, around five shedding cycles are represented, corresponding to two turn-overs, with eddy turn-over time defined as L_x/U_{ref} , where L_x is the streamwise length of the domain and U_{ref} the inlet velocity. The number of gathered shedding periods is limited by the available computer power. Even if the number of shedding periods available for data processing is limited, their data allow to extract quantities sufficiently close to the experimental ones to label the present simulation as a partial success; the effects of the limited amount of sampled data on the presented results will be discussed case by case.

In Table IV the Strouhal number (St), the rms of c_l , the mean c_d and its rms are compared with the respective range of experimental values as extracted from Reference [4], while the length of the re-circulation bubble behind the obstacle is compared with the value extracted from Reference [8]. Due to the limited amount of shedding periods, the uncertainty

Table IV. Bulk coefficients for cylinder flow.

	St	c_l^{rms}	c_d	c_d^{rms}	l_r/H
<i>LES</i>	0.127	1.35	2.23	0.23	0.75
<i>EXP</i>	0.133	0.1–1.4	1.9–2.1	0.1–0.23	0.88

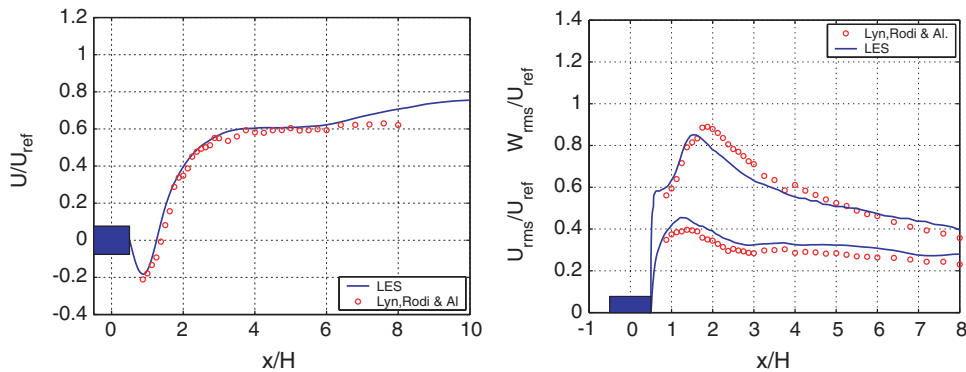


Figure 18. Mean streamwise velocity (left) and rms of streamwise and vertical velocity (right), at the centerline of the wake.

on St is high (± 0.01), but the experimental value falls well within the uncertainty range of present LES. For the other coefficients, for example c_d , it is still an open issue whether is necessary to apply the corrections developed in the experimental literature [27]. In the aforementioned workshop [4], no corrections were applied, and in Table IV the uncorrected coefficients are presented. As a matter of fact, it is not trivial to adapt the corrections suggested in Reference [27] to present data, due to the particular nature of the boundary conditions used.

From Table IV we see that the mean drag coefficient, possibly the most interesting information, is slightly over-estimated, a fact that is consistent with literature findings [4]. The other values present in general a good agreement, with the partial exception of the recirculation length l_r/H , which is slightly underestimated.

The distribution of c_p around the obstacle is also shown in Figure 17 and compared with two sets of experiments [4]. The following figures compare mean and rms velocities profiles of the present LES with the reference experiments of Lyn [8]; the comparisons are performed only in terms of long-time average, as no phase average [8] was currently available for the LES.

The first comparison presents, in Figure 18, the streamwise velocity along the wake centreline, as well as the corresponding rms of streamwise and vertical velocities. The results can be considered satisfactory, taking into account results of other LES simulations [4] carried out for the same benchmark. The two key trends of the wake are reasonably well reproduced; also the behaviour of the re-circulation bubble in terms of velocity minimum and length is respected, while the velocity defect in the near wake is well recovered.

An overview of the streamwise velocity profiles in the whole wake is presented in Figure 19 while their rms are presented in Figure 20; the graphs show the comparison between LES and all the experimental data for all measurement stations in the wake, from location $x/H = 5/8$

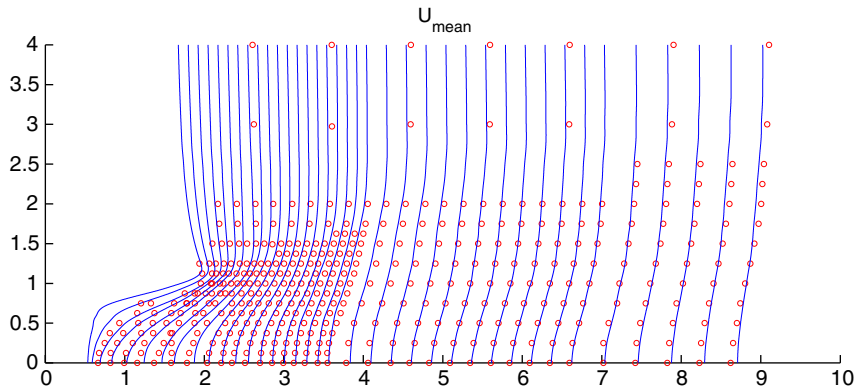


Figure 19. Evolution of the mean streamwise velocity in the wake.

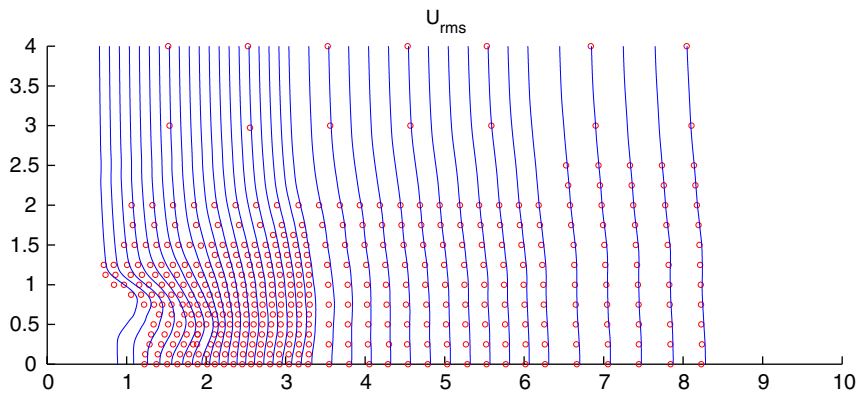


Figure 20. Evolution of the rms of the streamwise velocity in the wake.

until $x/H = 8$, x being the streamwise co-ordinate. For each profile, the abscissa corresponds to the value of the velocity for a given ordinate plus a displacement equal to its position in the wake (x/H).

An overall agreement is found over most of the development, indicating the capability of the present discretization to capture all the fundamental processes of this part of the flow field.

Concerning the simulation of the flow close to the cylinder, profiles of mean streamwise velocity and corresponding rms are shown for two locations in Figures 21 and 22; the first one shows the flow behaviour over the obstacle itself, while the second one is in the near wake, two diameters downstream the body. In Figure 21, it can be seen that the mean velocity and the rms are in good agreement with the experiments; concerning the rms profile, it must be remarked that it presents two separated maxima: the first one is related to the main shear layer on the obstacle, while the second one, close to the surface, is related to the wall dynamics.

In Figure 22, the mean velocity close to the wake centreline is still in good agreement with experiments, while sufficiently away from it, the mean velocity predicted by LES is lower than the experimental value; this disagreement is probably due to the different conditions for

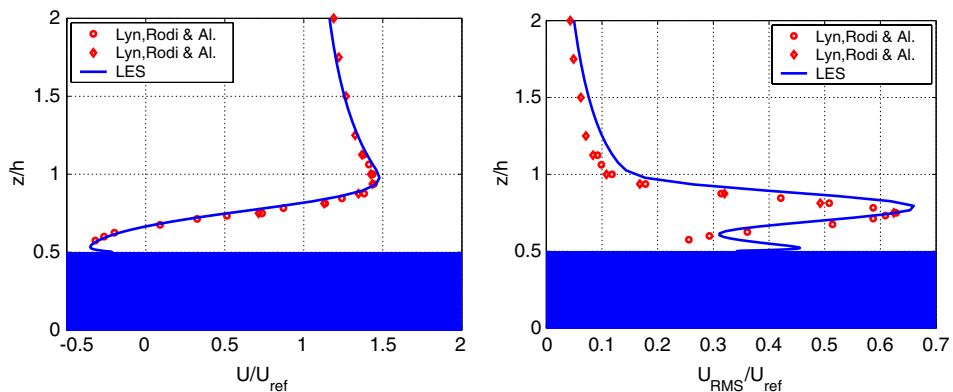


Figure 21. Mean streamwise velocity (left) and rms of the streamwise velocity (right) at $x/H = 1/4$.

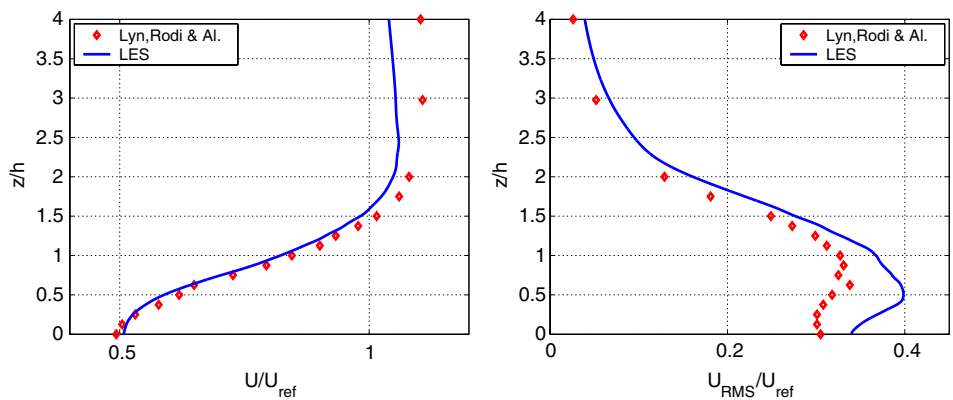


Figure 22. Mean streamwise velocity (left) and rms of the streamwise velocity (right) at $x/H = 5/2$.

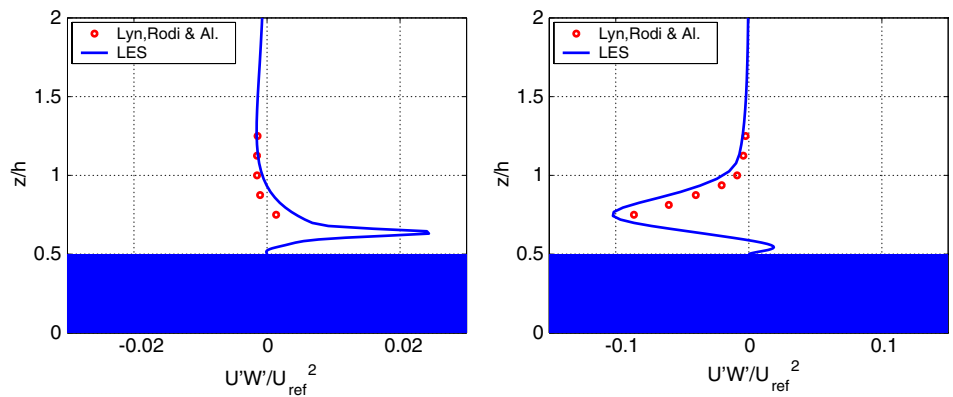


Figure 23. Turbulent shear stress at $x/H = -3/8$ (left) and $x/H = 3/8$ (right).

the upper and lower boundaries (see above), while the rms starts to deviate in magnitude, with respect to the experiments.

Finally, in Figure 23, the mean turbulent shear is presented for two positions, symmetric with respect to the centre of the obstacle; good agreement is still evident.

In conclusion, the higher complexity of this flow field and the higher Reynolds number has made it impossible to have a level of resolution and quality of agreement between present LES and reference data similar to the one found for the BFS case, but, overall, a satisfactory agreement is obtained, while the flexibility and the possibilities of the MD approach, in terms of adaptation of discretization schemes and turbulent models for different parts of the complex flow field, have been highlighted.

7. CONCLUSIONS

The present investigation has put in evidence the capabilities and the performance of the MD technique proposed in the companion paper [5] for LES of complex flows.

The algorithm has been shown to possess the ability to accurately describe very complex flow fields, and to achieve, through proper multi-domain partitioning, a local grid optimization. It also permits to introduce the most adequate discretization techniques and/or physical modes in different parts of the computational domain (Section 6), thus, making it ideally suitable for zonal approaches.

Results presented herein are confined to three-dimensional flows which are two-dimensional in the mean, but the extension to fully three-dimensional flows is immediate and it is presently undergoing implementation and testing. The generalization to non-Cartesian geometries, through the immersed boundary method is feasible and straightforward [28].

A further advantage of the present approach lies with its capability to resolve the inflow boundary condition problem associated with a spatially developing flow through a *concurrent pre-simulation inflow generator* technique. The above strategy, here applied to the simulation of a TBL (Section 4) and BFS (Section 5) flow, has been shown capable to yield remarkable results; specifically, the entrance length of the computational domain necessary to provide correct inflow data at a given location was significantly reduced ($< 5\delta_{inlet}$).

On the application side the simulation of BFS flow at moderate Reynolds number (Section 5) has outlined the efficiency of the MD approach, showing a satisfactory agreement of the resolved statistics with reference to DNS data with a remarkable computational saving. The simulation of the flow around a cylinder of square cross-section (Section 6) has confirmed these capabilities for more complex problems.

To conclude, present results represent a full validation of the methodology detailed in [5] and allow to propose it as a cost-effective and flexible solution to the simulation of more challenging flows.

ACKNOWLEDGEMENTS

The authors are indebted to the *Edinburgh parallel computing center (EPCC)*, who made generously available its Sun HPC 3500 super-computer, to Dr Simons during his TRACS research visit as a Ph.D. student, a training program on high-performance computing funded by the European Union's transnational access to research infrastructures programme. Professor Giulio Iannello of the *Università Campus Biomedico* of Rome provided valuable support when discussing several issues related to the parallel architecture.

Part of this research work was partially supported by the Office of Naval Research under Grant No. N00014-99-0834.

REFERENCES

1. Piomelli U. DNS and LES, basic principles, current trends, expectations. *Introduction to the Modelling of Turbulence*, von Kármán Institute Lecture Series, 2000-02. von Kármán Institute: Rhode S. Genese, Belgium, 2002.
2. Sagaut P. *Large eddy Simulation for Incompressible Flows*. Springer Scientific Computation. Springer-Verlag: Berlin, Germany, 2001.
3. Malan P. Turbulence modelling for industrial computational fluid dynamics. *Industrial Computational Fluid Dynamics*, von Kármán Institute Lecture Series, 1999-06. von Kármán Institute: Rhode S. Genese, Belgium, 1999.
4. Rodi W, Ferziger JH, Breuer M, Pourquié M. Status of large eddy simulation: results of a workshop. *Journal of Fluids Engineering* 1997; **119**:248–262.
5. Manna M, Simons E, Benocci C. Large eddy simulation of turbulent flows via domain decomposition techniques. Part 1: theory. *International Journal for Numerical Methods in Fluids* 2005, in press.
6. Le H, Moin P. Direct numerical simulation of turbulent flow over a backward-facing step. *Report TF-58*, Stanford University, December 1994.
7. AGARD. A selection of test cases for the validation of large eddy simulations of turbulent flows. *Agard Advisory Report 345*, North Atlantic Treaty Organization, Neuilly-Sur-Seine, France, April 1998.
8. Lyn DA, Einav S, Rodi W, Park JH. A laser-doppler velocimetry study of ensemble averaged characteristics of the turbulent near wake of square cylinder. *Journal of Fluid Mechanics* 1995; **304**:285–319.
9. Rai M, Moin P. Direct numerical simulation of transition and turbulence in a spatially evolving boundary layer. *Journal of Computational Physics* 1993; **109**:169–192.
10. Wallace JM, Eckelmann H, Brodkey RS. The wall region in turbulent shear flow. *Journal of Fluid Mechanics* 1972; **54**:39–48.
11. Townsend AA. *The Structure of Turbulent Shear Flow*. Cambridge University Press: Cambridge, 1976.
12. Hartel C, Kleiser L, Unger F, Friedrich R. Subgrid-scale energy transfer in the near-wall region of turbulent flows. *Physics of Fluids* 1994; **6**(9):3130–3143.
13. Kline SJ, Reynolds WC, Schrauband FA, Runstadler PW. The structure of turbulent boundary layer. *Journal of Fluid Mechanics* 1967; **50**:133–150.
14. Zang TA. Numerical simulation of the dynamics of turbulent boundary layers: perspectives of transition simulator. *Philosophical Transactions of the Royal Society of London Series A* 1991; 95–102.
15. Giammanco R, Benocci C. LES investigation of coherent structures in boundary layers and wakes, vol. I. *ONR Grant N00014-99-1-0834. Contract Report 2003-08*, von Kármán Institute for Fluid Dynamics, December 2003.
16. Chapman DR. Computational aerodynamics development and outlook. *AIAA Journal* 1979; **17**(12):1293–1311.
17. Piomelli U, Balaras EG. Wall-layer models for large-eddy simulations. *Annual Review of Fluid Mechanics* 2002; **34**:349–374.
18. Spalart PR. Direct numerical simulation of turbulent boundary layer up $Re_\theta = 1410$. *Journal of Fluid Mechanics* 1988; **187**:61–97.
19. Antonia RA, Teitel M, Kim J, Browne LWB. Low Reynolds number effects in a fully developed turbulent channel flow. *Journal of Fluid Mechanics* 1992; **236**:579–605.
20. Lund TS, Wu X, Squire KD. Generation of turbulent inflow data for spatially developing boundary layer simulations. *Journal of Computational Physics* 1998; **140**:233–258.
21. van Driest ER. On turbulent flow near a wall. *Journal of Aeronautical Science* 1956; **23**(11):1007–1011, 1036.
22. Schlichting H. *Boundary Layer Theory* (7th edn). McGraw-Hill: New York, 1979; 596–625.
23. Akselvoll K, Moin P. Large eddy simulation of turbulent confined coannular jets and turbulent flow over a backward facing step. *Report TF-63*, Stanford University, February 1995.
24. Jovic S, Driver DM. Backward facing step measurements at low Reynolds number $Re = 5000$. *Tm 108807*, NASA, 1994.
25. Kawamura T, Takami H, Kuwahara K. *New Higher Upwind Schemes for Incompressible Navier–Stokes Equations*, Lecture Notes in Physics, vol. 218. Springer: Berlin, 1984; 291–295.
26. Fureby C, Grinstein FF. Monotonically integrated large eddy simulation of free shear layers. *AIAA Journal* 1999; **37**(5):544–556.
27. AGARD. Wind tunnel wall corrections. *Agard Advisory Report 336*, North Atlantic Treaty Organization, Neuilly-Sur-Seine, France, October 1998.
28. Grosjes T. Simulation on general bodies on Cartesian grids: application to VKI-LES code. *Manual 57*, von Kármán Institute for Fluid Dynamics, May 2002.